# Decoding PARP1 Selectivity: Atomistic Insights for Next-Generation Cancer Inhibitors

Alejandro Feito,[1,2] Natàlia DeMoya-Valenzuela,[3] Cristian Privat,[3] Andrés R. Tejedor,[1,4,2] Lucía Paniagua-Herranz,[3] Adrian Garaizar,[5] Alberto Ocana,[3,a)] and Jorge R. Espinosa[1,4,2,b)]

[1)] *Department of Physical Chemistry, Universidad Complutense de Madrid, Av. Complutense s/n, Madrid 28040, Spain*

[2)] *Instituto Pluridisciplinar, Universidad Complutense de Madrid, P.º de Juan XXIII, 1, Moncloa - Aravaca, 28040 Madrid, Spain*

[3)] *Experimental Therapeutics Unit, Hospital Clínico San Carlos (HCSC), Instituto de Investigación Sanitaria San Carlos (IdISSC), Madrid, Spain*

[4)] *Yusuf Hamied Department of Chemistry, University of Cambridge, Lensfield Road, Cambridge CB2 1EW, UK*

[5)] *Data Science, Bayer AG, Germany*

(Dated: 15 October 2025)

Selective inhibition of PARP1 has emerged as a promising strategy to improve the therapeutic index of PARP inhibitors, a class of anticancer agents that exploit defects in DNA repair pathways. While PARP inhibitors have shown remarkable clinical benefit, particularly in BRCA-mutated tumors, the lack of discrimination between PARP1 and its close homolog PARP2 often leads to hematological toxicity and limits treatment efficacy. Therefore, achieving molecular selectivity for PARP1 remains a central challenge in the rational design of safer and more potent inhibitors. Here, we perform atomistic molecular dynamics simulations using potential of mean force (PMF) calculations, energetic decomposition, and targeted in silico mutagenesis to dissect the molecular determinants underlying PARP1 versus PARP2 selectivity across four representative approved compounds. Our simulations of the catalytic domain were used to quantify residue–ligand contact frequencies, ligand-induced modulation of protein flexibility, and the free-energy landscapes governing binding and unbinding processes. Contact analysis identified key residues mediating ligand recognition, while energetic decomposition characterized the dominant stabilizing forces inducing ligand-protein interactions. Importantly, our PMF profiles revealed distinct energetic and molecular features of association pathways responsible for ligand selectivity. Our results demonstrate that selective inhibitors stabilize unique PARP1 interactions and follow favorable low-barrier association routes, whereas the same ligands encounter higher barriers in PARP2. Together, these findings provide a unified mechanistic framework for selectivity and inform the design of next-generation PARP1 inhibitors with improved efficacy and safety.

Keywords: PARP inhibitors — molecular dynamics — protein-ligand binding — data-driven drug discovery

## I. INTRODUCTION

Poly(ADP-ribose) polymerase 1 (PARP1) and 2 (PARP2) are nuclear enzymes that play an essential role in the detection and repair of DNA damage[1,2], particularly single-strand breaks[3]. Acting as key guardians of genomic integrity, they orchestrate a coordinated response to DNA lesions that ensures efficient repair[2], preserves chromatin organization[2], and maintains cellular viability[4]. Upon detection of DNA damage, PARP1 and PARP2 catalyze the polymerization of poly(ADP-ribose) chains and recruit other nuclear factors to promote chromatin remodeling[5–7] and the assembly of DNA repair complexes[8]. Beyond their canonical role in DNA repair, PARP1 and PARP2 contribute to transcriptional regulation[9], replication fork stability[10], and cellular responses to oxidative stress[11], underscoring their broad involvement in nuclear homeostasis. Their activity is crucial for maintaining genomic stability, and defects in these pathways—such as those resulting from *BRCA1/2* mutations[12,13]—are tightly linked to oncogenesis[14–18]. The central role of PARP1 and PARP2 in DNA damage sensing and repair therefore makes them compelling targets for therapeutic intervention, particularly in tumors dependent on compensatory repair mechanisms for survival[19,20].

Targeting PARP1 and PARP2 with small-molecule inhibitors has become an effective therapeutic strategy[21–24], exploiting synthetic lethality in cancers with homologous recombination (HR) repair deficiency[25,26]. Clinically approved PARP inhibitors—including olaparib[27–29], rucaparib[30,31], niraparib[32,33], and talazoparib[34,35]—inhibit both PARP1 and PARP2. This lack of selectivity contributes to a narrow therapeutic window and characteristic hematologic toxicities largely attributed to PARP2 inhibition[14,29,36]. Next-generation inhibitors such as saruparib[37] and NMS-P118[38] were designed to achieve higher PARP1 selectivity, thereby minimizing adverse hematologic effects[39] and emphasizing the clinical importance of selective targeting[18]. Developing highly selective PARP1 inhibitors not only promises im-

[a)] Electronic mail: alberto.ocana@salud.madrid.org

[b)] Electronic mail: jorgerene@ucm.es

proved tolerability but also enables rational combination therapies with DNA-damaging agents under a safer therapeutic profile[40]. Although both saruparib and NMS-P118 were conceived as PARP1-selective inhibitors, their clinical outcomes differ: NMS-P118 displayed approximately 150-fold selectivity over PARP2 and remained preclinical[38], whereas saruparib exhibits up to 500-fold selectivity[41], enhanced hematologic safety, and has advanced to clinical trials[42], showing durable responses in HR-deficient tumors[18].

Understanding the molecular basis of inhibitor selectivity requires detailed knowledge of how these drugs interact with specific amino acid residues within the binding site (i.e., the catalytic site), as well as with accessory factors such as HPF1[43,44], which modulate enzymatic activity[18,45–47]. Although high-resolution structural data provide essential configurations of these interactions, they often fail to capture the conformational dynamics and solvent effects critical for predicting binding affinity and specificity[48,49]. Atomistic molecular dynamics (MD) simulations[50–54] can successfully address these limitations by describing inhibitor binding at atomic resolution in an explicitly solvated media and dynamically evolving environment at physiological conditions. By characterizing the conformational flexibility of the active site, identifying key residue contacts, and quantifying binding energy landscapes, MD simulations bridge static structural information with the dynamic behavior of biomolecular systems. Unlike crystallographic models, these simulations incorporate solvent, ions, and conformational ensembles, yielding a realistic picture of ligand–protein recognition. Such computational frameworks enable dissection of the energetic and structural determinants underlying potency and selectivity, allowing systematic testing of hypotheses that are often inaccessible experimentally. In this way, molecular simulations not only guide rational drug design and optimization of existing inhibitors but can also accelerate the discovery of new compounds with improved efficacy and safety.

In this study, we performed atomistic MD simulations of wild-type PARP1 and PARP2 catalytic domains in complex with a representative set of inhibitors, including PARP1-selective compounds (NMS-P118[38] and saruparib[37]) and non-selective inhibitors (olaparib[27] and veliparib[27,55]). Key protein–ligand interactions are characterized by monitoring residue-level contacts within the catalytic site, while binding energetics were quantified through potential of mean force (PMF) calculations. Furthermore, we evaluate the structural variability of PARP1 and PARP2 in their wild-type state and upon ligand binding using root-mean-square deviation (RMSD) and root-mean-square fluctuation (RMSF) analyses. To further probe the contribution of individual residues to ligand recognition, we also performed targeted mutagenesis of highly interacting residues to glycine, with particular emphasis on contacts formed with the selective inhibitor saruparib. Our integrative approach combines dynamic, energetic, and mutational analyses to unveil the molecular determinants that govern binding affinity and selectivity, providing a framework for the rational improvement of next-generation PARP inhibitors.

## RESULTS AND DISCUSSION

The specific binding of molecular inhibitors to PARP1 aims to alter its catalytic function by blocking and/or modulating its local conformation and intramolecular interactions. To establish a baseline, we first characterized the structure and intramolecular interactions of the unbound protein using MD simulations. All-atom simulations were performed employing the a99SB-*disp* force field and the TIP4P-*disp* water model[56,57] under physiological conditions (310 K, 150 mM NaCl; see Sections SI and SII of the Supplementary Material (SM) for further details). These simulations provided atomistic insights into the conformational ensemble of full-length wild-type PARP1, yielding a single-protein radius of gyration ($R_g$) of 69 ± 6 Å (Fig. S1 and Section SIV for analysis details) . To further assess the robustness of these results and cross-check conformational sampling, we also performed simulations using the coarse-grained (CG)[58] residue-resolution model Mpipi Recharged[59] (see Section SIII in the SM for model details). This model has been shown to accurately reproduce the conformational behavior of diverse protein systems across a wide range of temperatures and salt concentrations[59–61]. CG simulations carried out under the same conditions yielded an $R_g$ of 70 ± 1 Å, in close agreement with the all-atom results. Because the experimental $R_g$ values for PARP1 obtained from small-angle X-ray scattering (SAXS) measurements[62] were determined at 277 K and 50 mM NaCl—conditions at which all-atom simulations are difficult to equilibrate—we used the Mpipi Recharged model to compute the $R_g$ under these conditions. The resulting average value of 57 ± 1 Å is in consistent agreement with the SAXS value of 56.7 Å[62], supporting the reliability of the model and its consistency with the all-atom simulations at 310 K. The corresponding $R_g$ distributions are shown in Figure S1 of the SM. Overall, both the all-atom and coarse-grained simulations yielded compatible $R_g$ values (Fig. S1) that are also consistent with experimental SAXS measurements, demonstrating the agreement between approaches and validating the Mpipi Recharged model and, indirectly, the a99SB-*disp* all-atom simulations against experimental data.

Since atomistic simulations of full-length PARP1 (1002 residues) are computationally demanding due to the large system size required to avoid self-interaction through periodic boundary conditions (see Section SI for details), we next explored whether simulations of the active site alone—where small-molecule inhibitors bind—can preserve the same folded structure observed in the full-sequence simulations. To this end, we performed all-atom MD simulations under physiological conditions for both

full-length PARP1 and PARP2, as well as for their corresponding active sites alone. From the obtained trajectories, we computed intramolecular contact maps (see Section SV in the SM for details) to identify the key interactions stabilizing the protein folding patterns (see Fig. S2 in the SM). As shown in Figure S2, the contact patterns within the active sites of both PARP1 and PARP2 remained largely unchanged relative to those in the full-length proteins. This behavior likely arises from their globular architecture and the limited number of long-range interactions with other regions, which allow their overall conformation to remain self-sustained. Therefore, we restrict our subsequent atomistic simulations to the ∼260 C-terminal residues encompassing the catalytic domains, as this provides an efficient and reliable strategy to investigate the interaction mechanisms of PARP1 and PARP2 with various drug candidates under physiological conditions at notably lower computational cost.

### Ligand-protein contact analysis of PARP inhibitors in PARP1 and PARP2

Understanding the atomic-level interactions between small-molecule inhibitors and the active sites of PARP1 and PARP2 is essential for elucidating the molecular basis of selectivity. Consequently, we analyzed the contact frequencies between selected ligands and the active sites of both enzymes obtained from 1 microsecond atomistic simulations starting from the experimentally resolved PDB structures (see Section SV of the SM for further details). We selected two PARP1-specific inhibitors (NMS-P118[38] and saruparib[37]) and two non-selective inhibitors (olaparib[27] and veliparib[27,55]) to assess whether the resulting contact profiles can provide insights into drug selectivity. The force field parameters and topology for all ligands were derived using the OpenFF toolkit[63], ensuring compatibility with the all-atom simulations for the protein sequence using the a99SB-*disp* force field (see Section SI for further details). For each inhibitor, we computed the number of contacts between each heavy atom of the ligand and the center of mass of the side chain of each amino acid residue. A contact was defined to occur when this distance was less than approximately 6 Å (see Section SV for methodological details). This threshold was chosen to capture specific non-covalent interactions while ensuring meaningful binding (see the complete protein–ligand contact maps in Fig. S3 of the SM). The number of contacts per heavy atom was normalized by the highest frequency for each drug to enable comparison of the relative distribution of contacts across all inhibitors studied for both PARP1 (Fig. 1A–D) and PARP2 (Fig. 1E–H). Consequently, the relative contact score ranges from 0 to 100 (%), represented on a rainbow color scale. A summary of the most relevant residues contacting each molecule is provided in Table IA for PARP1 and Table IB for PARP2. Notably, only interactions that persisted for more than 80% of the total simulation time were included, ensuring that the reported contacts are both stable and functionally relevant.

In Figure 1A, we present the normalized contact map for NMS-P118 interacting with the catalytic domain of PARP1. The atoms exhibiting the highest contact frequency are located within the fluorinated aromatic group (C2–C1–C4) and the amide moiety (C6–O28–N19). The fluorinated ring predominantly interacts with LYS903 through cation-*pi* interactions, consistent with the positive charge of the lysine side chain. In addition, the fluorinated group frequently contacts GLU988, which—although counterintuitive given the negative charge of glutamate—likely results from a specific conformational arrangement of the protein that brings GLU988 in close spatial proximity to the ligand despite its charge. The amide moiety also engages in multiple polar interactions with SER904, HIS862, and GLY863. Moreover, NMS-P118 forms $\pi$–$\pi$ stacking interactions with several tyrosine residues (TYR889, TYR896, and TYR907), which likely contribute to the ligand's residence time within the active site and, consequently, to its overall binding affinity. Notably, residues HIS862, GLY863, TYR889, TYR896, ALA898, LYS903, SER904, and TYR907 maintained contacts for more than 80% of the total simulation time (see Table IA), in agreement with static X-ray crystallographic structures of the corresponding ligand–protein complexes[38]. This consistency supports the structural predictions of our MD simulations.

Next, we present the contact frequency analysis between PARP1 and saruparib (Figure 1B). In this case, the region of the ligand exhibiting the highest frequency of contacts is centered around the aromatic ring at the lower portion of the molecule (C12–C16 and N3). Importantly, the most frequent and persistent interactions with the catalytic pocket involve the same residues observed for NMS-P118—namely HIS862, GLY863, ALA898, LYS903, SER904, TYR896, and TYR907—suggesting a conserved binding mode driven by several key non-bonded interactions despite structural differences among the ligands (see Table IA). In contrast, the tail region of saruparib displays distinct non-bonded interaction patterns not present in NMS-P118. Specifically, the amino groups on the non-aromatic rings within this region form stable contacts with the side chains of ASP766 and ASP770. Moreover, the terminal amide group (centered on C17) engages in electrostatic interactions with ARG878, further stabilizing the ligand within the binding pocket. These additional polar contacts may enhance the overall binding affinity and contribute to the distinct specificity profile of saruparib compared to other PARP inhibitors. Importantly, the interactions identified from our simulations are consistent with those observed in X-ray crystallographic structures—ASP770, HIS862, GLY863, ARG878, ILE879, SER904, and TYR907—of the PARP1–saruparib complex[37]. Notably, our MD simulations also reveal additional transient contacts arising from the intrinsic flexibility of both the protein and the ligand such as ASP776, LEU769, ALA880, PRO881,

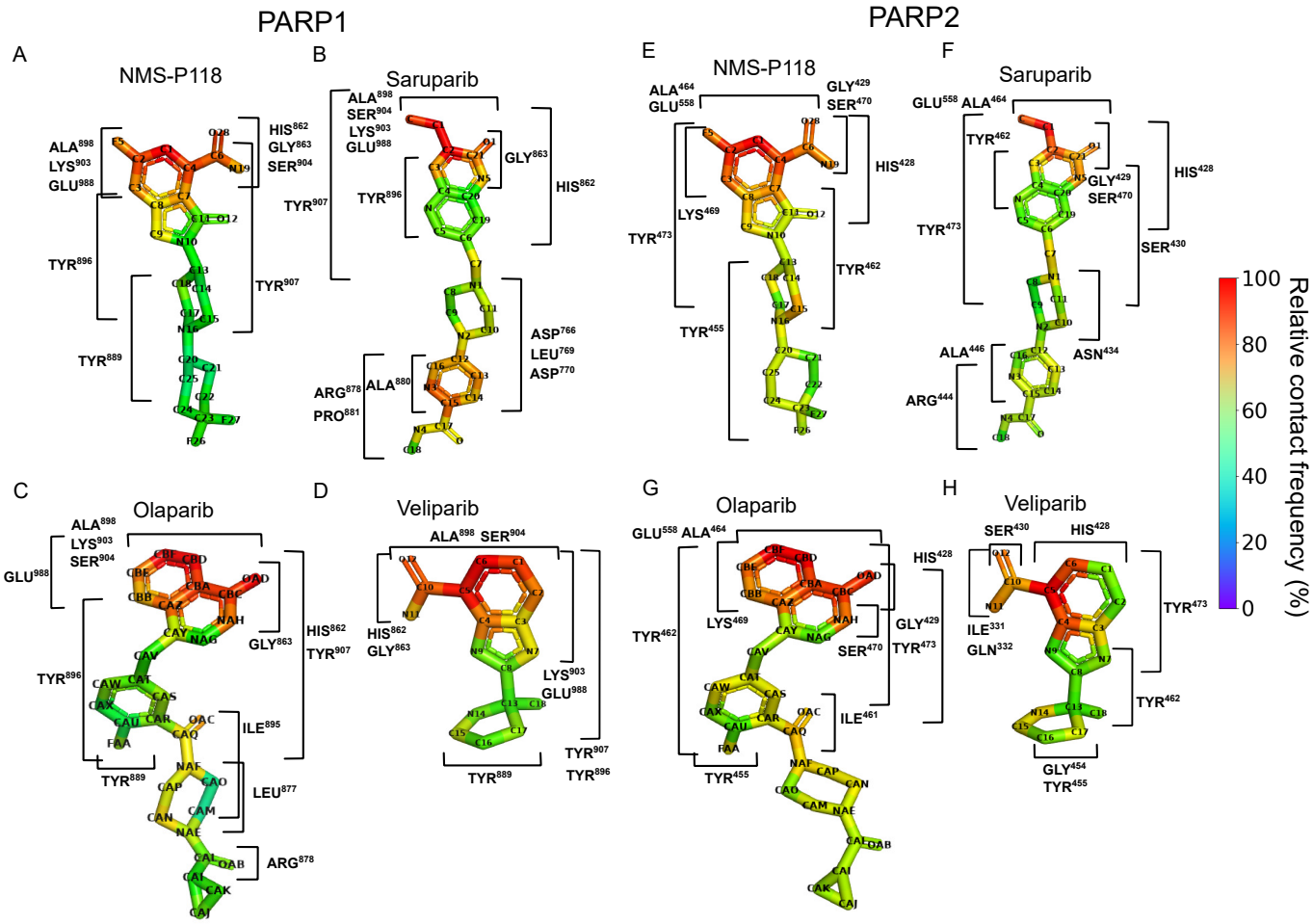


FIG. 1. Relative contact frequency (%) of the PARP inhibitors saruparib (A), NMS-P118 (B), olaparib (C), and veliparib (D) with PARP1 and with PARP2 (saruparib (E), NMS-P118 (F), olaparib (G), and veliparib (H)) within the catalytic binding site.

TYR896, ALA898, LYS903, and GLU988—features not fully captured in static crystallographic snapshots. This observation highlights the added value of atomistic simulations in identifying time-dependent interactions that, while dynamically fluctuating, contribute to the stability and specificity of the binding interface.

In Figure 1C, we now present the interaction profile between olaparib and the catalytic domain of PARP1. The overall contact pattern closely resembles that of saruparib, reflecting the structural similarities between the two molecules, including their shared interaction with ARG878 (see Table IA and Fig. 1A,C). However, olaparib also displays specific interactions that distinguish its binding mode from that of saruparib. In particular, olaparib forms a $\pi$–$\pi$ stacking interaction with TYR889 through its fluorinated aromatic ring (CAU–CAT–FAA), similar to that observed for NMS-P118 but with lower persistence (see the fourth row in Table IA). Additionally, olaparib establishes unique hydrophobic contacts with LEU877 and ILE895, further supporting its binding through non-polar interactions specific to its chemical structure. Nevertheless, the strong binding affinity of the lower aromatic ring of saruparib (i.e., C12–C16 and N3) is not present in the terminal end of olaparib exhibiting only moderately binding probability of ∼50%. While X-ray crystallography has resolved several of the key interactions—particularly those involving catalytic residues[27] (GLY863 and TYR907)—our atomistic MD simulations also provide a more comprehensive depiction of the binding interface including key interactions such HIS862, TYR889, ALA898, TYR896, LYS903, SER904 and GLU988.

We also analyzed the contact profile between veliparib and the catalytic domain of PARP1 (Fig. 1D). The binding mode of veliparib is characterized by extensive $\pi$–$\pi$ stacking interactions involving the aromatic residues TYR889, TYR896, and TYR907, which are distributed along the length of the ligand due to its smaller molecular size compared to the other inhibitors. These interactions contribute significantly to stabilizing the molecule within the binding pocket and suggest a binding mechanism predominantly governed by aromatic stacking. In

addition, the analysis reveals that the most frequent contacts are concentrated around the core of the ligand (i.e., the bicyclic aromatic rings, C1–C6, and the C10-centered amide), corresponding to its most reactive region and further supporting the presence of a canonical binding mode shared among several PARP inhibitors (see Table IA). The persistent nature of these core interactions, together with the distributed $\pi$–$\pi$ stacking, likely enhances the overall affinity and anchoring of veliparib within the active site.

Similarly, Figures 1E–H present the contact analyses between PARP2 and the inhibitors NMS-P118 (E), saruparib (F), olaparib (G), and veliparib (H). Overall, the interaction profiles closely resemble those observed for PARP1, involving comparable types of non-covalent contacts with homologous aromatic and polar residues within the binding pocket. Notably, when focusing on the selective molecules (i.e., NMS-P118 and saruparib), their interaction distributions appear more homogeneous. This effect likely reflects intrinsic differences in the binding interface, which in PARP2 is slightly more extended and permissive, thereby enabling interactions with the central regions of these ligands. Importantly, for all PARP2–ligand complexes except for NMS-P118, the maximum contact frequency is lower than in the corresponding PARP1 complexes. In the case of NMS-P118, however, a broader contact distribution is maintained, suggesting genuine structural differences in ligand engagement that may contribute to the binding behavior. An exception to this overall trend is observed with saruparib, where contacts involving the pyridinecarboxamide moiety—less buried within the active site—are markedly reduced. Thus, while these inhibitors display broadly similar binding modes between PARP1 and PARP2, the subtle variations in contact distribution indicate that contact analysis alone is insufficient to explain ligand selectivity and should be interpreted alongside complementary structural and dynamical information.

Analogously, Table IB lists the residues that consistently interact with all inhibitors in complex with PARP2. In contrast to PARP1, only a limited set of residues—specifically HIS428, TYR462, and TYR473 form common contacts across all ligands, suggesting a more restricted conserved interaction core within the PARP2 binding pocket. As with the PARP1 analysis, grouping the ligands according to their PARP1 selectivity does not reveal any distinctive contact patterns exclusive to either selective or non-selective compounds. Nonetheless, certain trends emerge within different subgroups. For instance, NMS-P118 and the non-selective inhibitors all interact with TYR455, while saruparib and the non-selective compounds share contacts with SER430. Interestingly, a broader set of shared contacts is observed between the PARP1-selective inhibitors and olaparib, including residues such as GLY429, ALA464, LYS469, SER470, and GLU558. This overlap suggests that olaparib may partially mimic the interaction profile of PARP1-selective inhibitors within PARP2, potentially explaining its relatively balanced affinity for both protein paralogs.

To further validate the reliability of the active-site simulations, we calculated contact maps for PARP1 bound to saruparib and PARP2 bound to veliparib using the last $\sim$350 residues of each protein, instead of only the 260 C-terminal catalytic domain as previously performed. This extended construct includes the adjacent $\alpha$-helical regulatory domain (see Figure S4 in the SM). The results show that, for saruparib, the contact map remains virtually unchanged, confirming that truncating the protein at such level barely modifies the observed interaction network. In contrast, for veliparib, a minimal loss of contacts is observed near the extreme C-terminal region, which is considerably more flexible in the truncated construct than in the full-length protein. This enhanced flexibility permits transient interactions between the ligand and distal regions to form more readily within shorter simulation times, suggesting that the observed contacts in the truncated system likely represent a conservative estimate of the full range of possible binding interactions.

Overall, our contact analysis reveals notable differences in how each ligand interacts with PARP1 and PARP2—in terms of residue identity and spatial distribution—however, these differences alone are insufficient to fully explain the chemical selectivity exhibited by certain inhibitors. Hence, although both common and ligand-specific contacts can be identified, no clear pattern emerges when grouping compounds by their selectivity profiles. Thus, a static or even time-averaged contact-based approach, while informative, does not capture the full complexity of the molecular determinants underlying inhibitor specificity. Nevertheless, this analysis provides valuable insights into the dynamic nature of protein–ligand recognition by identifying key residues that consistently engage in stabilizing interactions throughout the simulations—some of which have not been previously detected in the corresponding X-ray structures. Furthermore, it highlights key regions within the binding pockets of both PARP1 and PARP2 where interactions are primarily concentrated, thereby laying the groundwork for future studies that incorporate additional biophysical and energetic descriptors to better elucidate the mechanisms driving selective inhibition.

#### Binding Interaction Analysis of PARP Inhibitors

To further characterize the nature of the protein–ligand interactions, we next performed a per-residue binding free energy decomposition for PARP1, aimed at identifying the dominant stabilizing forces and comparing how different inhibitors engage the catalytic pocket. This analysis resolves the specific energetic contributions from van der Waals (vdW), electrostatic (El), and solvation terms, the latter separated into polar solvent (PS) and non-polar solvent (NPS) components, thereby providing a quantitative description of the energetic ba-

A

| PARP1 | NMS-P118 | Saruparib | Olaparib | Veliparib |
|---|---|---|---|---|
| IC in all inhibitors | HIS$^{862}$, GLY$^{863}$, TYR$^{896}$, ALA$^{898}$, LYS$^{903}$, SER$^{904}$, TYR$^{907}$, GLU$^{988}$ | | | |
| Common IC in different inhibitors | TYR$^{889}$ | | TYR$^{889}$ | TYR$^{889}$ |
| | | ARG$^{878}$ | ARG$^{878}$ | |
| Specific IC of each inhibitor | | ASP$^{766}$, LEU$^{769}$, ASP$^{770}$, ALA$^{880}$, PRO$^{881}$ | LEU$^{877}$, ILE$^{895}$ | |

B

| PARP2 | NMS-P118 | Saruparib | Olaparib | Veliparib |
|---|---|---|---|---|
| IC in all inhibitors | HIS$^{428}$, TYR$^{462}$, TYR$^{473}$ | | | |
| Common IC in different inhibitors | TYR$^{455}$ | | TYR$^{455}$ | TYR$^{455}$ |
| | | SER$^{430}$ | SER$^{430}$ | SER$^{430}$ |
| | GLY$^{429}$, ALA$^{464}$, LYS$^{469}$, SER$^{470}$, GLU$^{558}$ | GLY$^{429}$, ALA$^{464}$, LYS$^{469}$, SER$^{470}$, GLU$^{558}$ | GLY$^{429}$, ALA$^{464}$, LYS$^{469}$, SER$^{470}$, GLU$^{558}$ | |
| Specific IC of each inhibitor | | ASN$^{434}$, ARG$^{444}$, ALA$^{446}$ | ILE$^{461}$ | ILE$^{331}$, GLN$^{332}$, GLY$^{454}$ |

High contact frequency  Medium contact frequency  Low contact frequency

TABLE I. Key intermolecular contacts (IC) between the different inhibitors and PARP1 (A) or PARP2 (B) amino acids. Residues are colored according to the number of heavy-atom contacts established with the ligand: red indicates residues forming more than six contacts, orange corresponds to residues forming three to six contacts, and green highlights those forming one to three contacts. Rows indicate residue categories: contact residues present in all complexes, common residues among different inhibitors, and specific residue contacts of each inhibitor.

sis underlying inhibitor binding. The decomposition was carried out using the MMPBSA approach (see Section SVI in the SM for details). Our results are summarized in Figure 2, which depicts both the spatial distribution of key energetic contributors mapped onto the protein surface (left panels) and the residue-specific energy components (right panels).

For the NMS-P118 complex (Figure 2A), the strongest contributions arise from the aromatic residues TYR889, TYR896, and TYR907, primarily through van der Waals interactions, complemented by electrostatic stabilization from HIS862, GLY863, and GLU988. LYS903 also contributes through polar solvation effects that help secure the ligand within the catalytic site. In the olaparib complex (Figure 2B), the same tyrosine triad (TYR889, TYR896, TYR907) again dominates, although additional stabilization arises from ARG847 and GLU988, reflecting the distinct geometry of the olaparib scaffold. Saruparib (Figure 2C) engages the same canonical tyrosine residues, but a broader network of interactions is observed, with ASP766, ASN767, and LEU769 also providing stabilizing contributions, consistent with its extended contact surface within the pocket. Finally, veliparib (Figure 2D) maintains the general pattern of tyrosine-centered van der Waals stabilization, while electrostatic contributions from HIS862 and polar solvation effects from LYS903 are comparatively more pronounced, balancing the overall energetic signature. Across all complexes, van der Waals interactions consistently emerge as the predominant stabilizing force, supported by residue-specific electrostatic contributions and, to a lesser extent, by polar solvation. In contrast, non-polar solvation contributions are negligible in most of the cases, with values generally close to the threshold of 1 kcal/mol. This uniform energetic profile underscores that PARP1–ligand binding is largely driven by shape complementarity and localized polar interactions rather than by hydrophobic desolvation. Nevertheless, subtle differences in residue-level contributions—such as the broader stabilization network in saruparib or the enhanced polar solvation terms in veliparib—highlight how small variations in chemical structure can fine-tune the energetic landscape of binding.

The same binding free energy decomposition was performed for PARP2 (see Figure S5). The average binding free energies for all inhibitors are shown in Figures S6A and S7A for PARP1 and PARP2 respectively, while the residue-level energetic contributions are detailed in Figures S6B-D and S7B-D. Our analysis reveals that the energetic landscapes of PARP1 and PARP2 are strikingly similar. In both proteins, the dominant stabilizing forces arise from van der Waals interactions, primarily mediated by the conserved tyrosine triad (TYR889, TYR896, and TYR907 in PARP1; TYR462, TYR473, and TYR455 in PARP2), together with secondary contributions from HIS862, GLY863, and GLU988 (HIS428, GLY429, and GLU558 in PARP2). Polar solvation terms associated with LYS903 (LYS469 in PARP2) also provide measurable stabilization, whereas non-polar solvation contributions remain negligible in all cases. When comparing inhibitors, no major differences are detected either in the average interaction energies or in the residue-specific decomposition profiles (Figures S6 and S7), or in the hydrogen bonds analysis (Figure S8). Both selective and non-selective inhibitors seem to engage the same set of residues with comparable energetic balance, and the relative weighting between van der Waals and electrostatic components remains largely consistent across different ligands.

This outcome reinforces the conclusion that residue-level binding free energy analysis, while highly informative for identifying the residues that stabilize the complex, does not by itself provide a mechanistic basis to explain selectivity. Instead, selectivity likely arises from more subtle (i.e., entropic or cooperative effects) and/or long-range features of protein dynamics and conformational adaptation, which are not captured by energetic decomposition of an MD trajectory. Moreover, since our analysis was restricted to protein–ligand interactions

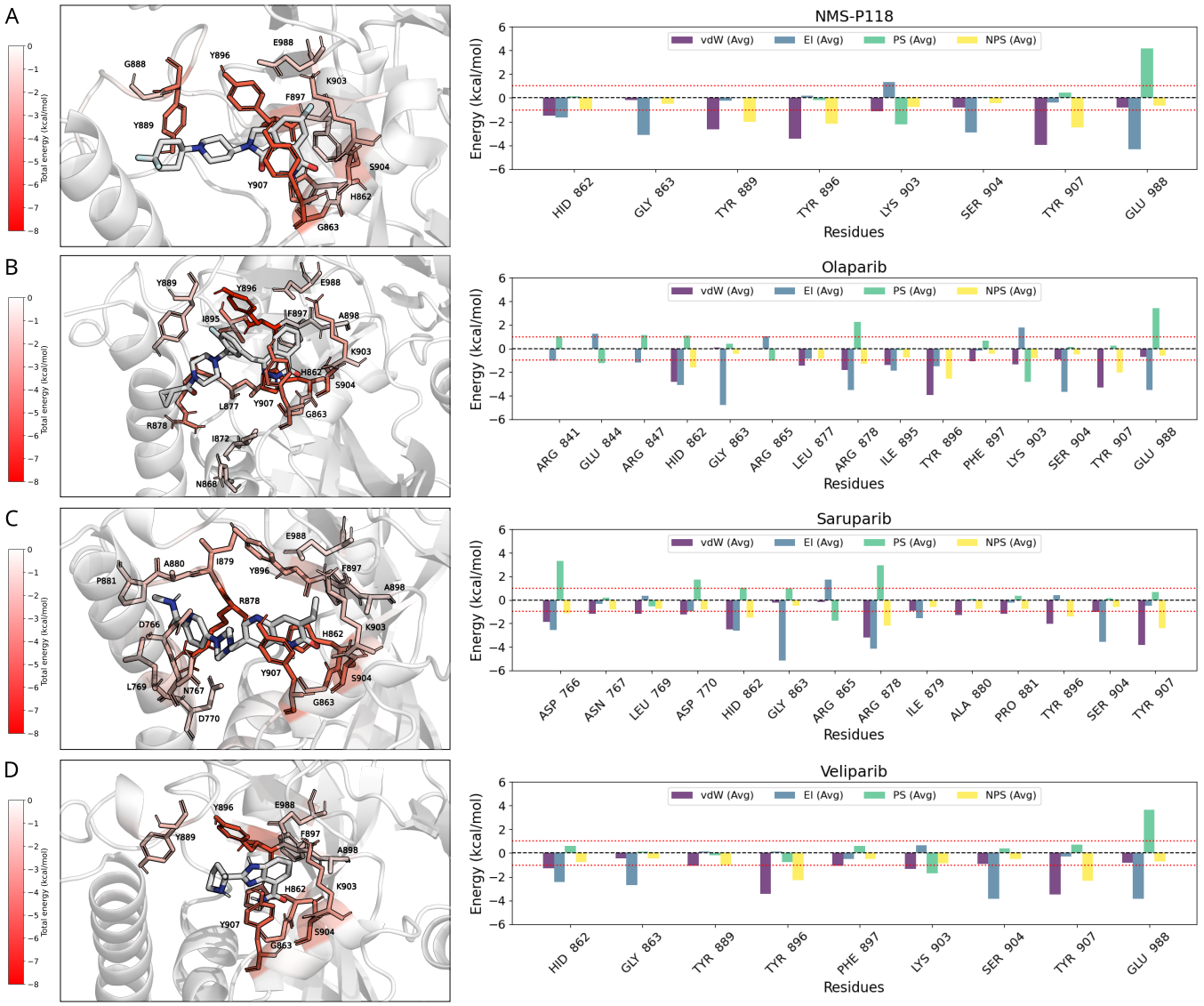


FIG. 2. Binding-site energy decomposition for PARP1 in complex with NMS-P118 (A), olaparib (B), saruparib (C), and veliparib (D). The inhibitors are depicted in white while the identified interactions of the residues through a colour map. Left panels: per-residue binding free energy decomposition mapped onto the protein surface, colored from low (white) to high (red) energetic contribution (kcal/mol). Right panels: average residue-wise interaction energies between PARP1 and each inhibitor. Only residues with an absolute contribution greater than 1 kcal/mol are displayed. Energy components are decomposed into van der Waals (vdW, blue), electrostatic (El, purple), polar solvation (PS, green), and non-polar solvation (NPS, yellow) terms.

within the catalytic site, it inherently does not account for contributions from distal regions or global conformational effects that may also enforce specificity.

### Potential of Mean Force Analysis of PARP–Ligand Interactions: Insights into the Binding Mechanisms and Selectivity

To quantify the strength of protein–ligand binding interactions and to characterize the energetic pathway underlying inhibitor association within the active site, we performed PMF calculations using Umbrella Sampling (US) simulations[64–66] at 300 K and 150 mM NaCl. Unlike the previous analyses, which focused on the ligand already bound within the catalytic pocket, this approach enables us to evaluate the free energy profile of the association/dissociation process, capturing both the formation and dissociation of the complex. More specifically, PMF simulations provide a quantitative description of the free energy landscape along a defined reaction coordinate (the center-of-mass (COM) distance between the inhibitor and the binding pocket), revealing how the interaction energy evolves as the ligand approaches or moves away from the protein (see Section SII in the Supporting Material). In practice, we generated a series of pro-

tein–ligand configurations separated by incremental distances, referred to as US *windows*. For each window, US simulations were conducted to compute the corresponding free energy contribution, allowing us to construct the PMF profile as a function of the COM distance between the protein and ligand (Figure 3A). Typically, the PMF profile exhibits a pronounced energy minimum near the crystallographic binding distance, corresponding to the most stable complex configuration. As the ligand is progressively pulled away, the interaction energy increases and eventually plateaus near zero, indicating complete dissociation and the absence of specific interactions beyond those with the solution.

In Figure 3B–E, we present the PMF profiles for each ligand, including the corresponding curves for PARP1 and PARP2. The PMF profile of saruparib (Figure 3B) reveals a marked contrast between the two enzymes. For PARP1 (maroon curve), the interaction is highly stabilizing, with a well depth of approximately -17.5 kcal/mol. The profile displays a smooth energy landscape, with moderately favorable interaction energies at intermediate distances along the reaction coordinate, suggesting the presence of transient encounter states that may facilitate a guided approach of the ligand toward the active site. In sharp contrast, the PMF for saruparib with PARP2 (light green dashed curve) exhibits only a shallow minimum of around 5.5 kcal/mol, considering the difference between this minimum and the corresponding energy barrier, an overall energetic gap of about $-4.8$ kcal/mol can be observed, indicative of a substantially weaker association and reduced propensity for stable binding. It is important to note that this PARP2–saruparib complex was constructed by aligning the protein structure to position the ligand within the active site, as no experimental structure is currently available. While this modeled configuration may not correspond to the absolute minimum-energy pose, the sufficiently long pre-equilibration runs preceding US simulations (e.g., 1 microsecond) should allow the relaxation toward the optimal energetically favorable conformation. Nonetheless, within the uncertainty of these calculations ($\sim$1 kcal/mol) the pronounced energetic difference between the PARP1 and PARP2 profiles provides strong computational support for the experimentally observed selectivity of saruparib toward PARP1 over PARP2[41].

An equivalent analysis was conducted for NMS-P118 (Figure 3C). The PMF for PARP1 (orange curve) exhibits a deep energy minimum of approximately -16.6 kcal/mol, indicative of high binding affinity. The energy landscape is relatively flat, showing significantly low barriers at intermediate distances (1–2 Å) along the reaction coordinate, suggesting a distinct association pathway compared to that of saruparib. This observation is consistent with our RMSF analysis (Fig. S9A and Section VII in SM for further details), which shows that NMS-P118 does not form stabilizing contacts with dynamic structural elements such as the $\alpha$-helix F, leaving this region highly flexible. In contrast, the PMF for PARP2 (violet curve) reveals a markedly weaker binding affinity, with a shallow minimum of only -4.1 kcal/mol. Notably, this profile features a moderate energy barrier of approximately 2–3 kcal/mol at intermediate distances ($\sim$1 Å) that is absent in PARP1. Such barrier possibly reflects unfavorable desolvation effects and the energetic cost of displacing water molecules solvating the inhibitor prior to the formation of productive ligand–protein contacts, thereby hindering the association of NMS-P118 with PARP2. Although the final binding state remains moderately favorable, the combination of a weak minimum for PARP2 and a much higher binding association free energy for PARP1 explains the experimentally established selectivity of NMS-P118 for PARP1[38,67].

Next, we extended our PMF simulations to the non-selective inhibitors veliparib and olaparib to further elucidate their binding profiles and potential mechanistic differences in their association with PARP1 and PARP2. For veliparib (Figure 3D), the PMF profile for PARP1 (dark blue curve) exhibits an energy minimum of approximately -15.9 kcal/mol, indicating strong thermodynamic affinity for the active site. However, the curve also displays a noticeable energy barrier of about 4.5 kcal/mol at intermediate distances along the reaction coordinate, suggesting an energetic hindrance during the approach of the ligand. In contrast, the PMF for PARP2 (light blue curve) reveals a shallower minimum of -8.5 kcal/mol, accompanied by a smoother energy landscape at intermediate distances. Interestingly, a small local minimum appears around 1.2 nm, possibly corresponding to a metastable intermediate state that may facilitate ligand guidance toward the binding pocket. Such smoother energetic profile may enable an association process that is more accessible, partially compensating for the weaker thermodynamic stabilization and resulting in an effective binding which is not that different to that of PARP1. These observations suggest that the depth of the energy minimum alone might not fully describe binding behavior; rather, the overall shape of the PMF curve provides critical insights into the mechanistic pathway of ligand association. Collectively, these PMF energy landscapes rationalize, in part, the experimentally observed non-selectivity of veliparib, which efficiently inhibits both PARP1 and PARP2[68,69].

For olaparib (Figure 3E), the PMF profile for PARP1 (red curve) shows an energy minimum of -17.8 kcal/mol, while PARP2 (blue curve) exhibits a similarly deep minimum of -18.1 kcal/mol. Both curves gradually descend along the reaction coordinate, indicating low to moderate energy barriers and an overall smooth association pathway. Notably, the PARP2 curve displays a subtle local minimum at intermediate distances, suggesting transient interactions that may guide the ligand toward the active site and facilitate binding. The comparable depths of the energy wells in both proteins provide a clear mechanistic explanation for the lack of selectivity of olaparib, consistent with experimental observations[70].

Our results are broadly consistent with experimen-

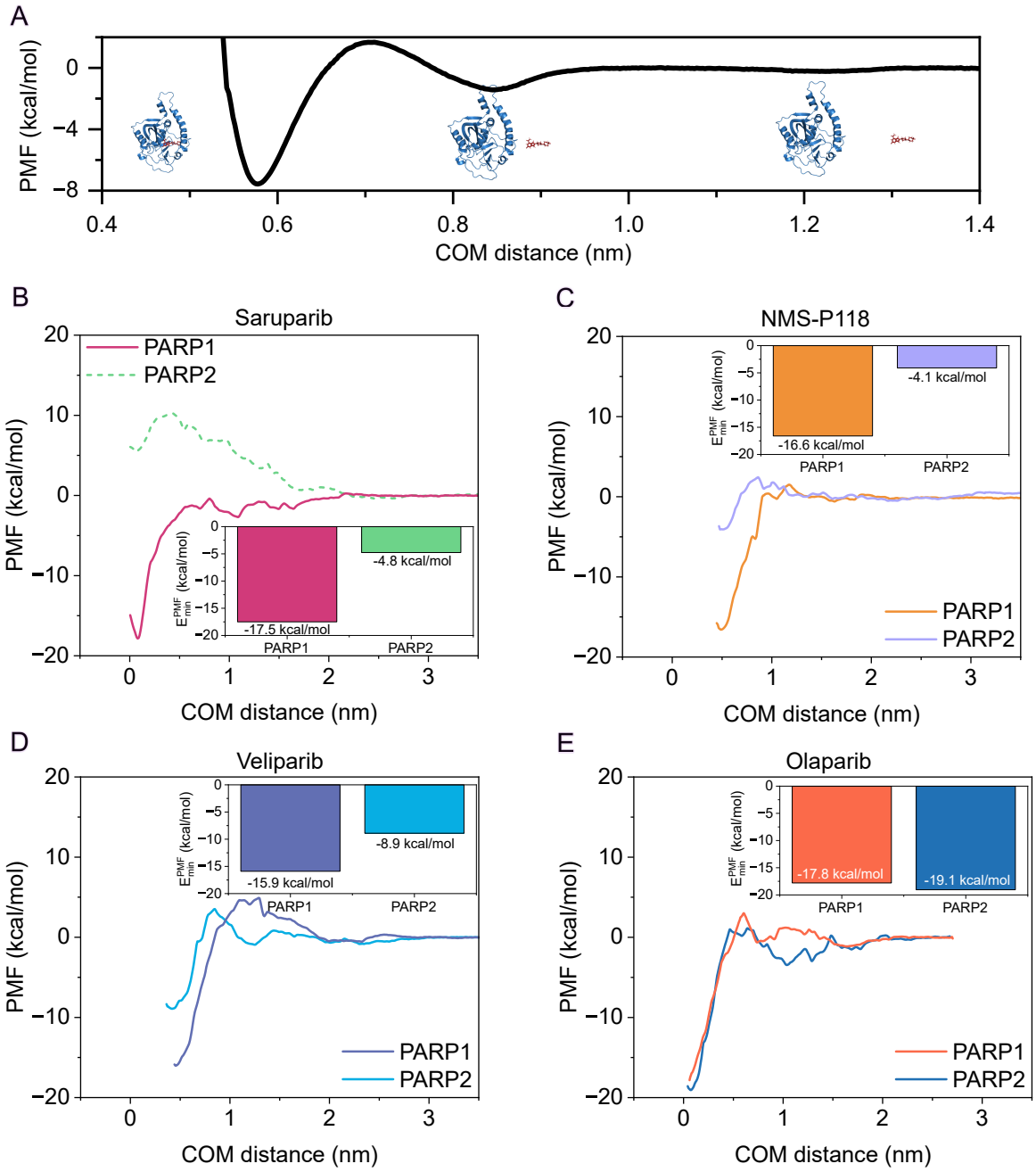


FIG. 3. (A) Schematic representation of a PMF profile between the protein and the ligand. Snapshots taken at different protein–ligand distances along the reaction coordinate are shown as insets. (B–E) Atomistic PMF dissociation profiles between each ligand and PARP1/PARP2 under physiological NaCl concentration (150 mM) and room conditions, in explicit solvent and ions, using the a99SB-disp force field. The center-of-mass (COM) distance between the protein and the ligand is used as the reaction coordinate. Curves are shown for saruparib (B), NMS-P118 (C), veliparib (D), and olaparib (E). Insets highlight the estimated minimum of the PMF for each complex, comparing PARP1 and PARP2. The dashed line of PARP2 with saruparib indicates that such configuration was generated through an MD trajectory rather than from equilibrated structurally resolved PDBs (for further details on the methodology please see section SI of the SM).

tal observations: both saruparib and NMS-P118 present much higher binding affinity for PARP1, veliparib has been reported to exhibit a modest preference for PARP1[71,72], while olaparib is generally considered non-selective[72,73]. At the same time, $IC_{50}$ measurements, the half maximal inhibitory concentration, indicate that in some studies both veliparib and olaparib show only limited PARP1 selectivity, and in certain contexts, even a relative preference for PARP2[67–70,72,74]. In Figure 4, we further provide a direct comparison between the binding

free energy values ($\Delta G$) obtained from our PMF profiles and those derived experimentally from $IC_{50}$ values using the following relation[75]:

$$\Delta G_{binding} = RT \ln(\mathrm{IC}_{50}(\mathrm{M})) \quad (1)$$

where $R$ is the gas constant, and $T = 300$ K. In Figure 2A, experimentally derived binding $\Delta G$ values are compared with those derived from the PMF profiles, revealing a qualitative correlation across the dataset. Experimental $IC_{50}$ values were taken as follows: saruparib, 3 nM for PARP1 (closed blue symbol) and 1400 nM for PARP2 (open blue)[41]; NMS-P118, 9 nM for PARP1 (closed red) and 1390 nM for PARP2 (open red)[38]; veliparib, 8.3 nM for PARP1 (closed green) and 11 nM for PARP2 (open green)[68]; and olaparib, 5 nM for PARP1 (closed orange) and 1 nM for PARP2 (open orange)[70] and then converted into binding $\Delta G$ values. We note that the absolute free energies quantitatively differ, experimental $\Delta G$ values range approximately from $-8$ to $-13$ kcal mol$^{-1}$, whereas PMF minima span from about $-20$ to $-5$ kcal mol$^{-1}$. This discrepancy likely arises from several potential sources: (1) inherent limitations of the force field[56]; (2) the positional restraints applied during the PMF calculations which constrain the ligand conformational freedom and may thus overstabilize the binding interaction strength in all systems[76]; and (3) the choice of the reaction coordinate for the dissociation pathway in the PMF calculations. The latter two factors may introduce a systematic offset that cannot be precisely quantified; therefore, the error bars in Fig. 4 reflect only the statistical uncertainty of our calculations. Nevertheless, despite these sources of uncertainty and our systematic offset (which would affect all systems equally) our simulations qualitatively reproduce the experimentally reported selectivity trends. Overall, the relative binding preferences between PARP1 and PARP2 are consistently captured, confirming that our PMF-based approach reliably reflects selectivity patterns even if the absolute free energies are offset. A similar trend to that shown in Figure 4 can also be observed in Figure S11, which compares the differences in $\Delta G_{\mathrm{binding}}$ between PARP1 and PARP2 for both the experimental and computational data sets.

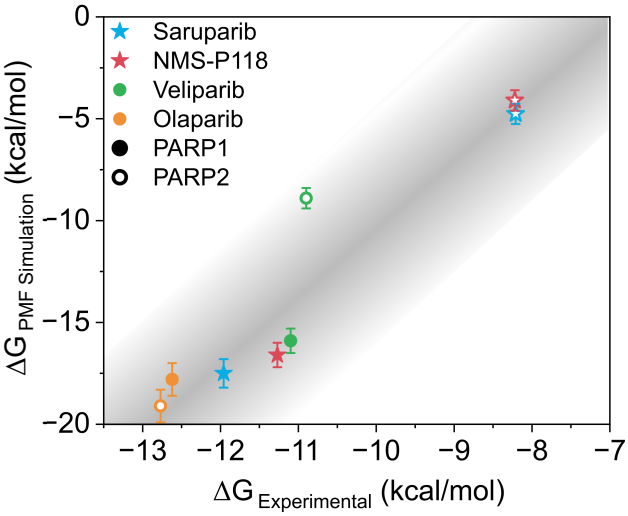


FIG. 4. Comparison between experimental ($\Delta G_{\mathrm{Experimental}}$) and simulated ($\Delta G_{\mathrm{PMF\ Simulation}}$) binding free energies for different inhibitors (Saruparib, NMS-P118, Veliparib, and Olaparib) for PARP1 and PARP2. A linear shading to the obtained correlation was added as a guide to the eye. Specific inhibitors of PARP1 are plotted in stars and non-specific inhibotrs in circles.

#### Impact of single-point mutations in PARP1-saruparib binding interaction strength

To gain deeper insight into the residue-level determinants of selective inhibitors of PARP1 such as saruparib, we performed a systematic mutational analysis targeting key amino acids within the active site. We have selected saruparib for these calculations over NMS-P118 not only due to its experimentally reported selectivity, but also because it exhibits several distinctive features: (1) it shows the most pronounced difference in PMF profiles between PARP1 and PARP2 (Fig. 3B); (2) it retains a high degree of PARP1 conformational flexibility (Fig. S9A); and (3) it forms a broad set of intermolecular contacts (Fig. IA), particularly involving its core and tail regions. These features make saruparib the most informative model among the different tested inhibitors to dissect the residue specific contributions of binding. The mutated residues are selected based on contact frequency—specifically those within the active site forming interactions with the largest number of heavy atoms in saruparib. This criterion provides a complementary view of binding determinants, as mutating these residues to glycine is expected to simultaneously disrupt multiple protein–ligand contacts, thereby revealing the extent to which binding stability depends on a network of side-chain interactions. In particular, residues were chosen according to the number of contacts established with saruparib when measured from their $C_\alpha$ atom within a 6 Å cut-off, offering an alternative perspective to that presented in Fig. 1. By replacing the selected residues with glycine, side-chain contributions were minimized, allowing assessment of their roles in maintaining the integrity of the ligand-protein within the binding pocket. The targeted residues—LEU877, ARG878, ILE879, ILE895, and ASN906—were identified as major contributors, among few others, to saruparib binding. To systematically evaluate their energetic relevance, different mutation sets were generated, comprising simultaneous replacements of five, three, or two amino acids, thereby enabling a graded assessment of their collective impact on ligand stabilization. Contact maps of the active-site region for the wild-type and mutant complexes (Figures 5A–D) reveal pro-

nounced alterations in the protein–ligand interaction network. In the wild-type PARP1–saruparib complex (Figure 5A), an extensive network of close highly frequent contacts is observed, reflecting multiple cooperative stabilizing interactions between the ligand and surrounding residues across the pocket.

Mutation of five key residues to glycine (PARP1-5GLY mutant: LEU877, ARG878, ILE879, ILE895, and ASN906; Figure 5B) leads to a substantial reduction in ligand-protein contacts across the catalytic site—which upon these mutations it maintains its overall structure—particularly affecting both the 877–879 segment and the 895–906 region. In the triple glycine mutant (PARP1-3GLY: LEU877, ARG878, ILE879; Figure 5C), the loss of contacts within the 877–879 region is retained, while interactions involving residues 895–906 are largely preserved. This indicates that the primary hotspot for stabilizing interactions resides within the 877–879 segment. The double glycine mutant (PARP1-2GLY: ILE895 and ASN906; Figure 5D) exhibits only a moderate reduction in interaction intensity, with the overall contact pattern remaining largely comparable to that of the wild-type complex (Figure 5A). The structural visualization of the active site (Figure 5E) highlights the mutated residues in red, illustrating their spatial arrangement within the binding cleft and their contribution to shaping the complementary surface accommodating saruparib. Collectively, these analyses suggest that while the binding interface is broadly distributed across the active site, the 877–879 segment represents a critical hotspot for stabilizing interactions, whereas other residues primarily modulate interaction strength without markedly altering the overall contact landscape.

Next, we quantify the variations in the interaction network found across the contact maps through PMF calculations, providing a detailed energetic description of the binding interaction strength for the wild-type and mutated PARP1 sequences in complex with saruparib. The resulting PMF profiles, depicted in Figure 5F, and their corresponding minimum values in Figure 5G, reveal a systematic modulation of the binding free energy landscape as a function of the number of glycine substitutions. The wild-type PARP1 complex (maroon curve) is characterized by a deep, well-defined global minimum of –17.5 kcal/mol, reflecting a highly stable interaction driven by optimal complementarity between the ligand and the intact active site. The profile displays a smooth descent into the energy well, indicative of a smooth pathway for ligand association.

We find that while the introduction of mutations progressively diminishes the binding stability, the effect is not entirely uniform across the different mutants. The double glycine mutant (PARP1-2GLY, light blue curve) exhibits a well-defined minimum of –11.4 kcal/mol—shallower than the wild-type but still clearly favorable. Nevertheless, the reduction in depth by approximately 6 kcal/mol highlights the importance of these two residues controlling the binding affinity. Notably, the emergence of more pronounced energy barriers at intermediate distances suggests that the mutated residues may play a key role in favoring the ligand into the active site. In contrast, the triple mutant (PARP1-3GLY, green curve) displays a less stable minimum of –7.5 kcal/mol, reflecting the energetic contributions of the additional side chains to the final bound state. In this case, the dominant effect is not the emergence of intermediate barriers but rather a destabilization of the binding minimum itself, underscoring the significant role of these residues in maintaining the thermodynamic stability of the complex. Finally, the most severe energetic perturbation is observed for the quintuple mutant (PARP1-5GLY, orange curve), where both effects combine: the minimum rises further to –6.3 kcal/mol, and the PMF profile shows a more pronounced energy barrier preceding it. This indicates that the extensive loss of complementary interactions simultaneously weakens the final bound state and introduces significant hurdles to ligand attachment, likely associated with desolvation penalties triggered by the absence of stabilizing contacts.

Collectively, our PMF calculations demonstrate that the high-affinity binding of saruparib to PARP1 does not arise from a few critical interactions but rather emerges from a cooperative network of multiple residue-specific contacts. This conclusion is supported by the observation that mutating a single residue (ARG878) does not significantly alter the protein's interaction network and only slightly perturbs the overall protein–ligand binding energy (Figure S12). In contrast, simultaneous mutation of several key residues to glycine disrupts this network in a cumulative manner, impacting the thermodynamics of binding. This detailed energetic mapping provides a molecular foundation for understanding structure–activity relationships, and offers mechanistic guidance for the rational design of inhibitors with enhanced selectivity. For completeness, the full set of contact maps for the mutant complexes is presented in Figure S13.

## CONCLUSIONS

In this work, we present an atomistic view of how four representative PARP inhibitors engage PARP1 and PARP2, and how these interactions collectively determine selectivity. By performing atomistic MD simulations and computing contact frequency maps, energy decomposition analyses, Umbrella Sampling potential-of-mean-force calculations, and targeted mutational perturbations, we demonstrate that selectivity is not a single intrinsic property, but rather an emergent outcome of multiple factors: the cooperative network of contacts anchoring the ligand within the pocket, the ligand-dependent modulation of the protein conformational ensemble, and the binding free energy landscape, which governs both the thermodynamic stability and accessibility of the binding process.

Our contact frequency maps reveal common recogni-

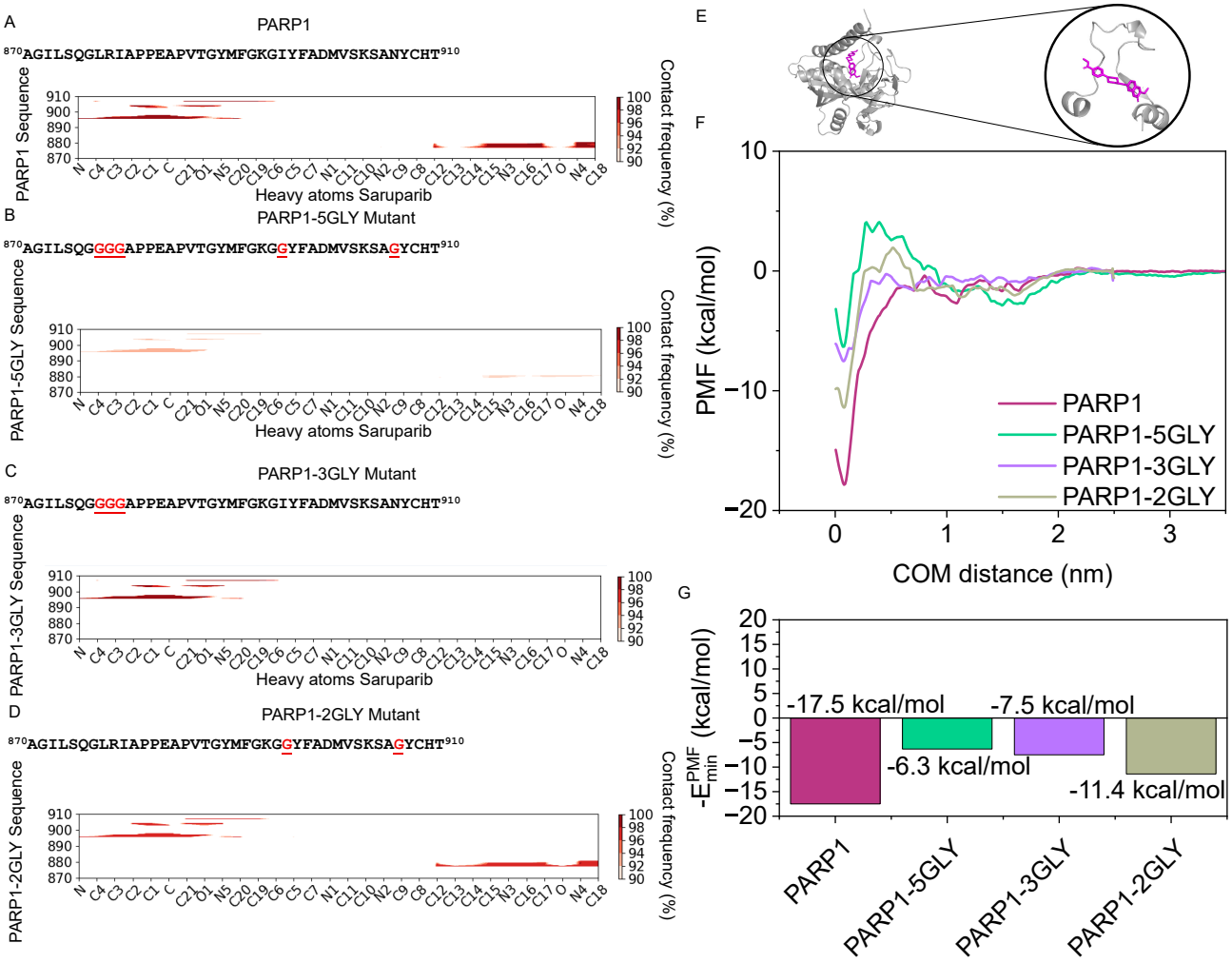


FIG. 5. Residue–ligand contact frequency maps for saruparib bound to PARP1 (A) and its glycine-substituted variants: 5GLY (B), 3GLY (C), and 2GLY (D). The PARP1 sequence region corresponding to residues 870–910 is shown above each map, with glycine substitution sites highlighted in red. Contact frequencies were calculated between heavy atoms of saruparib and the indicated protein residues. (E) Cartoon representation of the PARP1 active site in complex with saruparib. (F) PMF profiles for saruparib unbinding from PARP1 and the glycine mutants (5GLY, 3GLY, and 2GLY), computed as a function of the center-of-mass distance between the ligand and the protein. (G) Comparison of minimum binding free energy values derived from the PMF curves in (F).

tion motifs shared among different inhibitors, yet this feature alone is insufficient to explain why some compounds are selective while others are not. In our view, what distinguishes selective inhibitors is not merely which residues they engage, but how those interactions are dynamically organized and how they reshape the protein's conformational ensemble (Fig. S9). In this context, selective compounds seem to act cooperatively in two ways: they establish a dense, synergistic network of stabilizing interactions within the catalytic pocket, and they bring together the surrounding structural scaffold to create a more constrained and productive binding environment. However, predicting ligand selectivity solely through contact frequency analysis or energy decomposition remains challenging (Figs. 1 and 2).

In that sense, PMF profiling helps clarify the mechanistic basis of selectivity (Fig. 3). Selective inhibitors display binding landscapes that not only favor the formation of the desired complex but also introduce energetic barriers that hinder association with the non-target paralog, whereas non-selective compounds exhibit smoother energy surfaces that facilitate association with both proteins. In other words, specificity can be partially encoded in the topology of the association pathway rather than solely in the thermodynamic stability of the endpoint. Notably, comparison of PMF-derived $\Delta G$ values with experimental estimates obtained from $IC_{50}$ measurements reveals a notable correlation, indicating that the simulations reproduce the relative selectivity of the inhibitors despite systematic offsets in absolute free energies (Fig. 4).

This mechanistic picture carries direct implications for

drug design. Maximizing selectivity requires more than driving down the final binding free energy: it demands design choices that improve the approach pathway and that exploit interactions with structural elements adjacent to the pocket, to both deepen the desired bound state, and impede off-target association. Strategies that structurally bias attachment pathways by introducing interactions that stabilize productive intermediates may reduce off-target reactivity. In that sense, identifying the key contacts driving ligand-complex stabilization is fundamental to maximize specific binding. Our mutational perturbations make clear that selectivity strongly relies on multivalency rather than on single interaction modes (Fig. 5). Therefore, designing ligands that engage multiple complementary submotifs likely yields more durable protein-specific inhibitors. In this direction, we propose concrete experimental and computational follow-ups to translate and validate these principles using targeted mutagenesis of structural elements implicated in selectivity through kinetic binding assays to measure association/dissociation rates.

Taken together, our study highlights PARP inhibitor selectivity as an energy landscape problem: the critical question is not simply how tightly a ligand binds, but how the entire route to binding is organized and modulated by the ligand–protein interplay. By computing contact networks, conformational modulation of the protein binding site, and potential-of-mean force profiles of the association/dissociation pathways, we propose a computational framework to guide rational design of next-generation enzyme-selective inhibitors with improved efficacy and safety.

### Data availability

We provide the relevant data in the repository (GitHub link for the repository) to facilitate reproducibility of our results. In the repository we also give the necessary code to run the simulations and accessible instructions to obtain our results.

## ACKNOWLEDGMENTS

A. F. acknowledges funding from the Ramon y Cajal fellowship (RYC2021-030937-I) and Spanish National Grant (PID2022-136919NA-C33). A. R. T. acknowledges funding from the European Union Horizon 2020 research and innovation programme (grant agreement 803326 to R.C.-G.). J. R. E. acknowledges funding from Emmanuel College, the University of Cambridge, the Ramon y Cajal fellowship (RYC2021-030937-I), the Spanish scientific plan and committee for research reference PID2022-136919NA-C33, and the European Research Council (ERC) under the European Union's Horizon Europe research and innovation program (grant agreement no. 101160499). A.O., N.D.-V, C.P. and L.P.-H. acknowledge funding from CRIS Cancer Foundation (AOF.C01CRIS and AOF.M01CRIS). This work has also been performed using resources provided by Archer2 (https://www.archer2.ac.uk/) funded by EPSRC Tier-2 capital grant EP/P020259/e829. The authors also thankfully acknowledge RES computational resources provided by Mare Nostrum 5 through the activities 2024-3- 0001 and 2025-1-0009.

## BIBLIOGRAPHY

[1] H. L. Ko and E. C. Ren, Biomolecules **2**, 524 (2012).
[2] A. Ray Chaudhuri and A. Nussenzweig, Nature reviews Molecular cell biology **18**, 610 (2017).
[3] S. Eustermann, W.-F. Wu, M.-F. Langelier, J.-C. Yang, L. E. Easton, A. A. Riccio, J. M. Pascal, and D. Neuhaus, Molecular cell **60**, 742 (2015).
[4] G. E. Ronson, A. L. Piberger, M. R. Higgs, A. L. Olsen, G. S. Stewart, P. J. McHugh, E. Petermann, and N. D. Lakin, Nature communications **9**, 746 (2018).
[5] S. Sinha, S. Molla, and C. N. Kundu, Medical Oncology **38**, 118 (2021).
[6] W. Zong, Y. Gong, W. Sun, T. Li, and Z.-Q. Wang, Cancers **14**, 4162 (2022).
[7] E. E. Alemasova and O. I. Lavrik, Nucleic Acids Research **50**, 10817 (2022).
[8] Y.-C. Ho, C.-S. Ku, S.-S. Tsai, J.-L. Shiu, Y.-Z. Jiang, H. E. Miriam, H.-W. Zhang, Y.-T. Chen, W.-T. Chiu, S.-B. Chang, *et al.*, PLoS genetics **18**, e1010545 (2022).
[9] Y. Lu, W. Fu, W. Xing, H. Wu, C. Zhang, and D. Xu, Epigenetics & Chromatin **17**, 26 (2024).
[10] Y. Gong, Z. Wang, W. Zong, R. Shi, W. Sun, S. Wang, B. Peng, S. Takeda, Z.-Q. Wang, and X. Xu, Proceedings of the National Academy of Sciences **121**, e2322520121 (2024).
[11] K. Módis, D. Gerő, K. Erdélyi, P. Szoleczky, D. DeWitt, and C. Szabo, Biochemical pharmacology **83**, 633 (2012).
[12] I. Faraoni and G. Graziani, Cancers **10**, 487 (2018).
[13] S. Dilmac and B. Ozpolat, Cancers **15**, 3642 (2023).
[14] S. Boussios, P. Karihtala, M. Moschetta, C. Abson, A. Karathanasi, N. Zakynthinakis-Kyriakou, J. Ryan, M. Sheriff, E. Rassy, and N. Pavlidis, Investigational New Drugs **38**, 181 (2019).
[15] L. Cortesi, H. Rugo, and C. Jackisch, Targeted Oncology **16**, 255 (2021).
[16] Y. Zeng, O. Arisa, C. Peer, W. Figg, and A. Fojo, Seminars in oncology (2023), 10.1053/j.seminoncol.2023.09.005.
[17] P. G. Jain and B. D. Patel, European journal of medicinal chemistry **165**, 198 (2019).
[18] A. Herencia-Ropero, A. Llop-Guevara, A. D. Staniszewska, J. Domènech-Vivó, E. García-Galea, A. Moles-Fernández, F. Pedretti, H. Domènech, O. Rodríguez, M. Guzmán, *et al.*, Genome medicine **16**, 107 (2024).
[19] K. Yoshida and Y. Miki, Cancer science **95**, 866 (2004).
[20] M. Tarsounas and P. Sung, Nature Reviews Molecular Cell Biology **21**, 284 (2020).
[21] L. Cortesi, H. S. Rugo, and C. Jackisch, Targeted oncology **16**, 255 (2021).
[22] C. Y. Chan, K. V. Tan, and B. Cornelissen, Clinical Cancer Research **27**, 1585 (2021).
[23] D. Bhamidipati, J. I. Haro-Silerio, T. A. Yap, and N. Ngoi, British journal of cancer **129**, 904 (2023).
[24] J. Rudolph, K. Jung, and K. Luger, Proceedings of the National Academy of Sciences **119**, e2121979119 (2022).
[25] K. J. Rimar, P. T. Tran, R. S. Matulewicz, M. Hussain, and J. J. Meeks, Cancer **123**, 1912 (2017).

[26]H. L. Pálinkás, L. Pongor, M. Balajti, Á. Nagy, K. Nagy, A. Békési, G. Bianchini, B. G. Vértessy, and B. Győrffy, International Journal of Molecular Sciences **23**, 633 (2022).

[27]K. Ryan, B. Bolaños, M. Smith, P. B. Palde, P. D. Cuenca, T. L. VanArsdale, S. Niessen, L. Zhang, D. Behenna, M. A. Ornelas, *et al.*, Journal of Biological Chemistry **296** (2021).

[28]C. C. Gunderson and K. N. Moore, Future oncology **11**, 747 (2015).

[29]J. Murai, S.-Y. N. Huang, B. B. Das, A. Renaud, Y. Zhang, J. H. Doroshow, J. Ji, S. Takeda, and Y. Pommier, Cancer research **72**, 5588 (2012).

[30]L. Robillard, M. Nguyen, T. C. Harding, and A. D. Simmons, Cancer Research **77**, 2475 (2017).

[31]A. Musella, E. Bardhi, C. Marchetti, L. Vertechy, G. Santangelo, C. Sassu, F. Tomao, F. Rech, R. D'Amelio, M. Monti, *et al.*, Cancer Treatment Reviews **66**, 7 (2018).

[32]M. R. Mirza, B. J. Monk, J. Herrstedt, A. M. Oza, S. Mahner, A. Redondo, M. Fabbro, J. A. Ledermann, D. Lorusso, I. Vergote, *et al.*, New England Journal of Medicine **375**, 2154 (2016).

[33]A. González-Martín, B. Pothuri, I. Vergote, R. DePont Christensen, W. Graybill, M. R. Mirza, C. McCormick, D. Lorusso, P. Hoskins, G. Freyer, *et al.*, New England Journal of Medicine **381**, 2391 (2019).

[34]J. K. Litton, H. S. Rugo, J. Ettl, S. A. Hurvitz, A. Gonçalves, K.-H. Lee, L. Fehrenbacher, R. Yerushalmi, L. A. Mina, M. Martin, *et al.*, New England Journal of Medicine **379**, 753 (2018).

[35]N. Agarwal, A. A. Azad, J. Carles, A. P. Fay, N. Matsubara, D. Heinrich, C. Szczylik, U. De Giorgi, J. Y. Joung, P. C. Fong, *et al.*, The Lancet **402**, 291 (2023).

[36]Y. Shen, M. Aoyagi-Scharber, and B. Wang, The Journal of Pharmacology and Experimental Therapeutics **353**, 446 (2015).

[37]J. W. Johannes, A. Y. Balazs, D. Barratt, M. Bista, M. D. Chuba, S. Cosulich, S. E. Critchlow, S. L. Degorce, P. Di Fruscia, S. D. Edmondson, *et al.*, Journal of Medicinal Chemistry **67**, 21717 (2024).

[38]G. Papeo, H. Posteri, D. Borghi, A. A. Busel, F. Caprera, E. Casale, M. Ciomei, A. Cirla, E. Corti, M. D'Anello, *et al.*, Journal of medicinal chemistry **58**, 6875 (2015).

[39]C. J. LaFargue, G. Z. Dal Molin, A. K. Sood, and R. L. Coleman, The Lancet Oncology **20**, e15 (2019).

[40]J. Zheng, Z. Li, and W. Min, Frontiers in Pharmacology **13**, 979873 (2023).

[41]G. Illuzzi, A. D. Staniszewska, S. J. Gill, A. Pike, L. McWilliams, S. E. Critchlow, A. Cronin, S. Fawell, G. Hawthorne, K. Jamal, *et al.*, Clinical Cancer Research **28**, 4724 (2022).

[42]A. Azad, N. Agarwal, A. J. Armstrong, E. Hellmis, F. Schlürmann, M. Sugimoto, Y. Ürün, N. Xing, M. Aregay, J. Lima, *et al.*, "Phase iii, double-blind, placebo-controlled, 2-cohort, randomized study of saruparib (azd5305) in combination with androgen receptor pathway inhibitors in patients with metastatic hormone-sensitive prostate cancer with and without homologous recombination repair mutation (evoparprostate01)." (2025).

[43]I. Gibbs-Seymour, P. Fontana, J. G. M. Rack, and I. Ahel, Molecular cell **62**, 432 (2016).

[44]T. A. Kurgina, N. A. Moor, M. M. Kutuzov, K. N. Naumenko, A. A. Ukraintsev, and O. I. Lavrik, Communications biology **4**, 1259 (2021).

[45]J. Rudolph, G. Roberts, and K. Luger, Nature Communications **12** (2021), 10.1038/s41467-021-20998-8.

[46]A. Thorsell, T. Ekblad, T. Karlberg, M. Löw, A. Pinto, L. Trésaugues, M. Moche, M. S. Cohen, and H. Schüler, Journal of medicinal chemistry **60 4**, 1262 (2017).

[47]D. Bondar and Y. Karpichev, Biomolecules **14**, 1269 (2024).

[48]V. Limongelli, L. Marinelli, S. Cosconati, C. La Motta, S. Sartini, L. Mugnaini, F. Da Settimo, E. Novellino, and M. Parrinello, Proceedings of the National Academy of Sciences **109**, 1467 (2012).

[49]G. A. Ross, G. M. Morris, and P. C. Biggin, Journal of chemical theory and computation **9**, 4266 (2013).

[50]F. M. Aldakheel, S. A. Alduraywish, and K. H. Dabwan, Scientific Reports **15**, 12764 (2025).

[51]M. Khalid, M. H Alqarni, A. I. Foudah, and M. Saad Al Oraby, Journal of Biomolecular Structure and Dynamics , 1 (2025).

[52]J. Zhao, N. Yu, X. Zhao, W. Quan, and M. Shu, Journal of Molecular Modeling **29**, 131 (2023).

[53]H. Hu, B. Chen, D. Zheng, and G. Huang, PeerJ **8**, e9241 (2020).

[54]V. Nozal, O. Beyens, S. Peeters, A. Fabisiak, K. Augustyns, I. De Meester, P. Van der Veken, and H. De Winter, European Journal of Medicinal Chemistry , 117913 (2025).

[55]T. Karlberg, M. Hammarstrom, P. Schutz, L. Svensson, and H. Schuler, Biochemistry **49**, 1056 (2010).

[56]P. Robustelli, S. Piana, and D. E. Shaw, Proceedings of the National Academy of Sciences **115**, E4758 (2018).

[57]J. Aduriz-Arrizabalaga, X. Lopez, and D. De Sancho, Proteins: Structure, Function, and Bioinformatics **92**, 134 (2024).

[58]A. Šarić, Y. C. Chebaro, T. P. Knowles, and D. Frenkel, Proceedings of the National Academy of Sciences **111**, 17869 (2014).

[59]A. R. Tejedor, A. Aguirre Gonzalez, M. J. Maristany, P. Y. Chew, K. Russell, J. Ramirez, J. R. Espinosa, and R. Collepardo-Guevara, ACS Central Science **11**, 302 (2025).

[60]A. Feito, I. Sanchez-Burgos, A. Rey, R. Collepardo-Guevara, J. R. Espinosa, and A. R. Tejedor, Molecular Physics **122**, e2425757 (2024).

[61]A. Feito, I. Sanchez-Burgos, I. Tejero, E. Sanz, A. Rey, R. Collepardo-Guevara, A. R. Tejedor, and J. R. Espinosa, PLOS Computational Biology **21**, e1012737 (2025).

[62]S. O. Mansoorabadi, M. Wu, Z. Tao, P. Gao, S. V. Pingali, L. Guo, and H.-w. Liu, Biochemistry **53**, 1779 (2014).

[63]J. Wagner, M. Thompson, D. L. Mobley, J. Chodera, C. Bannan, A. Rizzi, trevorgokey, D. L. Dotson, J. A. Mitchell, jaimergp, Camila, P. Behara, C. Bayly, JoshHorton, L. Wang, I. Pulido, PEFrankel, V. Lim, S. Sasmal, J. A. Clark, SimonBoothroyd, A. Dalke, E. Holz, B. Westbrook, D. Smith, E. Pretti, J. Horton, and L.-P. Wang, "openforcefield/openff-toolkit: 0.16.9 minor release," (2025).

[64]A. Garaizar, J. R. Espinosa, J. A. Joseph, and R. Collepardo-Guevara, Scientific reports **12**, 4390 (2022).

[65]S. Blazquez, I. Sanchez-Burgos, J. Ramirez, T. Higginbotham, M. M. Conde, R. Collepardo-Guevara, A. R. Tejedor, and J. R. Espinosa, Advanced Science **10**, 2207742 (2023).

[66]A. R. Tejedor, I. Sanchez-Burgos, M. Estevez-Espinosa, A. Garaizar, R. Collepardo-Guevara, J. Ramirez, and J. R. Espinosa, Nature communications **13**, 5717 (2022).

[67]M. Petropoulos, A. Karamichali, G. G. Rossetti, A. Freudenmann, L. G. Iacovino, V. S. Dionellis, S. K. Sotiriou, and T. D. Halazonetis, Nature **628**, 433 (2024).

[68]S.-M. A. Huang, Y. M. Mishina, S. Liu, A. Cheung, F. Stegmeier, G. A. Michaud, O. Charlat, E. Wiellette, Y. Zhang, S. Wiessner, *et al.*, Nature **461**, 614 (2009).

[69]T. D. Penning, G.-D. Zhu, V. B. Gandhi, J. Gong, X. Liu, Y. Shi, V. Klinghofer, E. F. Johnson, C. K. Donawho, D. J. Frost, *et al.*, Journal of medicinal chemistry **52**, 514 (2009).

[70]K. A. Menear, C. Adcock, R. Boulter, X.-l. Cockcroft, L. Copsey, A. Cranston, K. J. Dillon, J. Drzewiecki, S. Garman, S. Gomez, *et al.*, Journal of medicinal chemistry **51**, 6581 (2008).

[71]J. Murai, Y. Zhang, J. Morris, J. Ji, S. Takeda, J. H. Doroshow, and Y. Pommier, The Journal of pharmacology and experimental therapeutics **349**, 408 (2014).

[72]J. W. Johannes, A. Balazs, D. Barratt, M. Bista, M. D. Chuba, S. Cosulich, S. E. Critchlow, S. L. Degorce, P. Di Fruscia, S. D. Edmondson, *et al.*, Journal of Medicinal Chemistry **64**, 14498 (2021).

[73]G. Kim, G. Ison, A. E. McKee, H. Zhang, S. Tang, T. Gwise, R. Sridhara, E. Lee, A. Tzou, R. Philip, *et al.*, Clinical cancer research **21**, 4257 (2015).

[74]J. D. Steffen, J. R. Brody, R. S. Armen, and J. M. Pascal, Frontiers in oncology **3**, 301 (2013).

[75]S. Holderbach, L. Adam, B. Jayaram, R. C. Wade, and G. Mukherjee, Frontiers in molecular biosciences **7**, 601065

(2020).

[76] A. Garaizar, J. R. Espinosa, J. A. Joseph, G. Krainer, Y. Shen, T. P. Knowles, and R. Collepardo-Guevara, Proceedings of the National Academy of Sciences **119**, e2119800119 (2022).

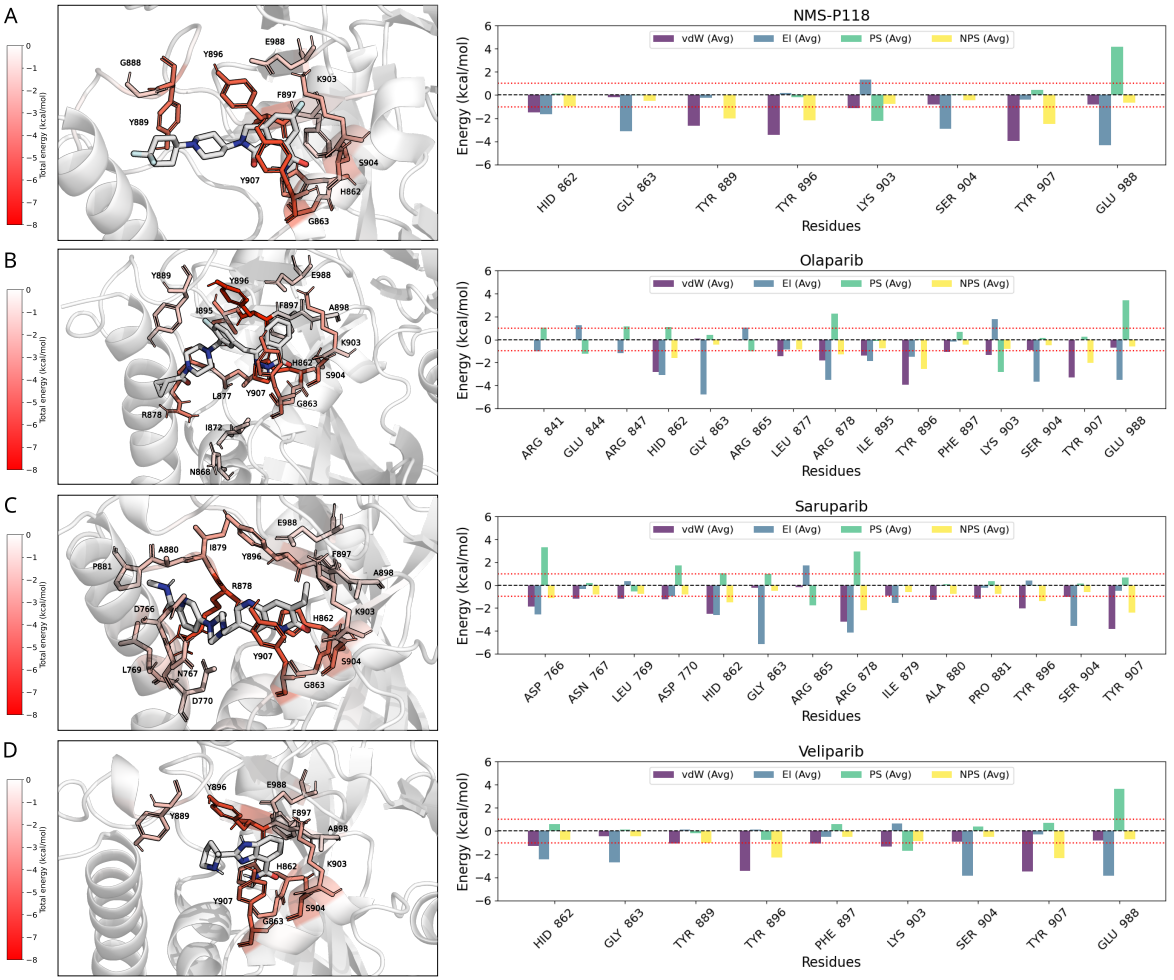
A
Total energy (kcal/mol)
0
−1
−2
−3
−4
−5
−6
−7
−8
G888
Y896
E988
K903
F897
Y889
S904
Y907
H862
G863
NMS-P118
vdW (Avg)
El (Avg)
PS (Avg)
NPS (Avg)
Energy (kcal/mol)
6
4
2
0
−2
−4
−6
HID 862
GLY 863
TYR 889
TYR 896
LYS 903
SER 904
TYR 907
GLU 988
Residues
B
Y889
Y896
E988
I895
F897
A898
K903
H862
S904
L877
Y907
G863
R878
I872
N868
Olaparib
ARG 841
GLU 844
ARG 847
HID 862
GLY 863
ARG 865
LEU 877
ARG 878
ILE 895
TYR 896
PHE 897
LYS 903
SER 904
TYR 907
GLU 988
C
E988
A880
I879
Y896
F897
P881
A898
R878
D766
H862
K903
Y907
S904
L769
N767
G863
D770
Saruparib
ASP 766
ASN 767
LEU 769
ASP 770
HID 862
GLY 863
ARG 865
ARG 878
ILE 879
ALA 880
PRO 881
TYR 896
SER 904
TYR 907
D
Y896
E988
Y889
F897
A898
H862
K903
Y907
S904
G863
Veliparib
HID 862
GLY 863
TYR 889
TYR 896
PHE 897
LYS 903
SER 904
TYR 907
GLU 988

A

| PARP1 | NMS-P118 | Saruparib | Olap |
|---|---|---|---|
| IC in all inhibitors | HIS$^{862}$, GLY$^{863}$, TYR$^{896}$, ALA$^{898}$, LYS$^{903}$, SE | | |
| Common IC in different inhibitors | TYR$^{889}$ | | TY |
| | | ARG$^{878}$ | AR |
| Specific IC of each inhibitor | | ASP$^{766}$, LEU$^{769}$, ASP$^{770}$, ALA$^{880}$, PRO$^{881}$ | LEU$^{87}$ |

High contact frequency

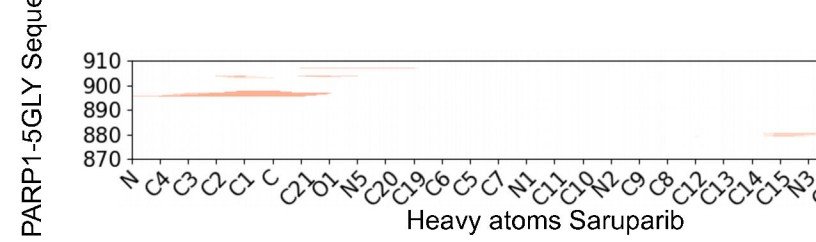


C

PARP1-3GLY Mutant

870AGILSQGGGGAPPEAPVTGYMFGKGIYFADMVSKSANYCHT910

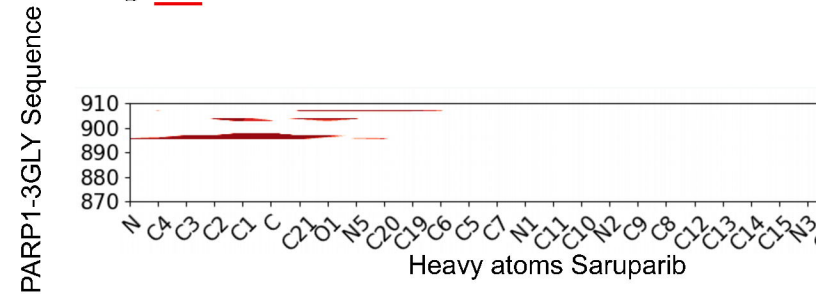


D

PARP1-2GLY Mutant

870AGILSQGLRIAPPEAPVTGYMFGKGGYFADMVSKSAGYCHT910

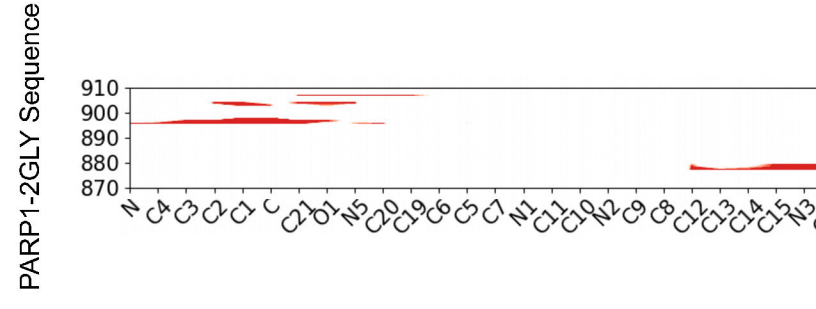

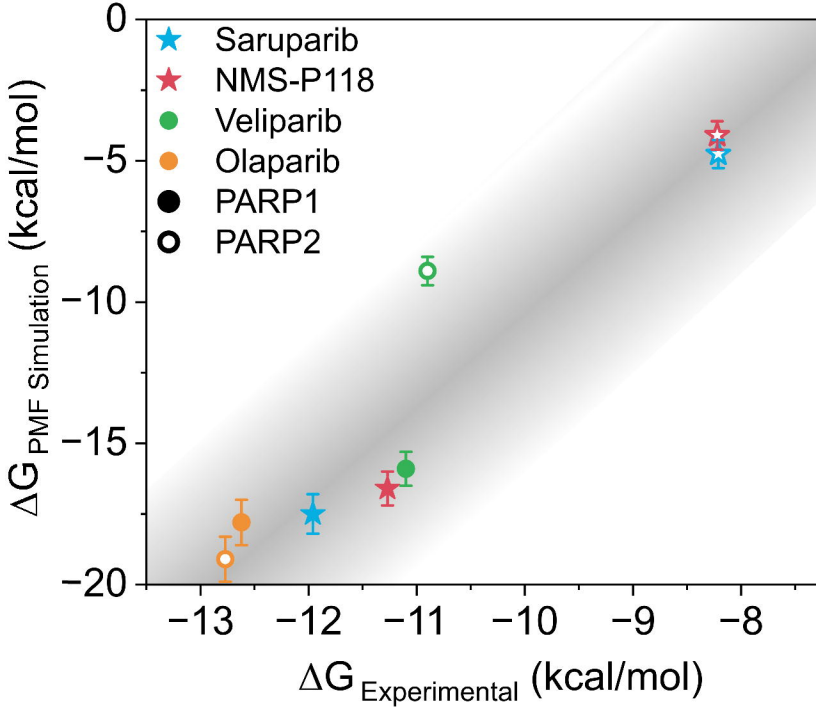
Saruparib
NMS-P118
Veliparib
Olaparib
PARP1
PARP2
0
−5
−10
−15
−20
−13
−12
−11
−10
−9
−8
ΔG PMF Simulation (kcal/mol)
ΔG Experimental (kcal/mol)

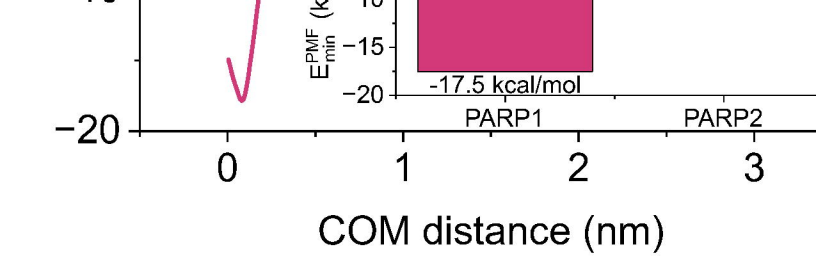
-17.5 kcal/mol
PARP1
PARP2
COM distance (nm)

D

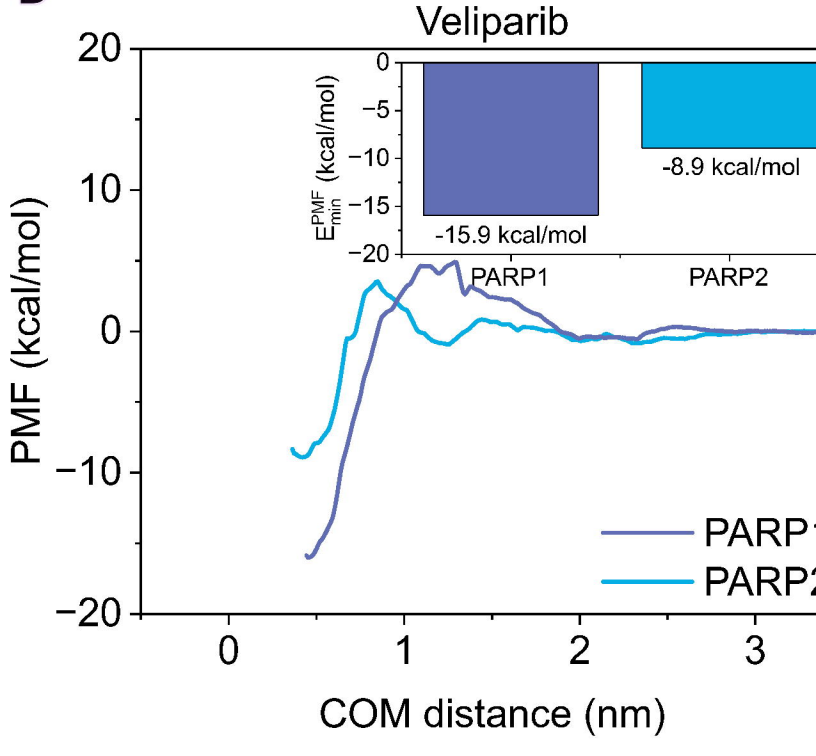
Veliparib
PMF (kcal/mol)
-15.9 kcal/mol
-8.9 kcal/mol
PARP1
PARP2
COM distance (nm)

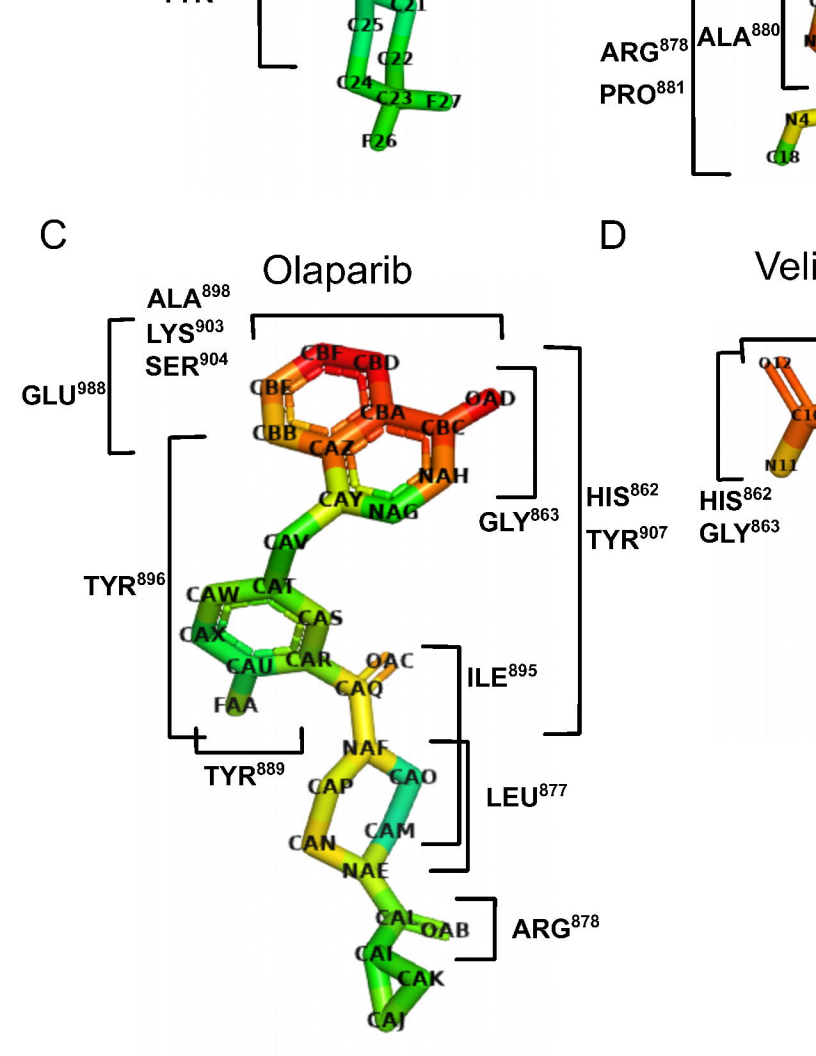
C21
C25
C22
C24
C23
F27
F26
ARG878
ALA880
PRO881
N4
C18
C
Olaparib
ALA898
LYS903
SER904
GLU988
CBF
CBD
CBE
OAD
CBA
CBC
CBB
CAZ
NAH
CAY
NAG
GLY863
HIS862
TYR907
CAV
TYR896
CAW
CAT
CAS
CAX
CAU
CAR
OAC
CAQ
FAA
ILE895
NAF
TYR889
CAP
CAO
LEU877
CAN
CAM
NAE
CAL
OAB
ARG878
CAI
CAK
CAJ
D
Veli
O12
C1
N11
HIS862
GLY863